Sulfur-induced greenhouse warming on early Mars

Sarah Stewart Johnson,[1] Michael A. Mischna,[2] Timothy L. Grove,[1] and Maria T. Zuber[1]

Received 2 July 2007; revised 12 December 2007; accepted 20 May 2008; published 8 August 2008.

[1] Mineralogical, geological, geophysical, and isotopic data recently returned from Mars suggest that the delivery of sulfur gases to the atmosphere may have played a significant role in the planet's early evolution. Using the Gusev Crater basalt composition and a batch melting model, we obtain a high sulfur solubility, approximately 1400 ppm, in Martian mantle melts. We proceed to explore different scenarios for the pulsed degassing of sulfur volatiles associated with the emplacement of near-surface dikes during the late Noachian or early Hesperian, when surface pressures are thought to be substantially higher than present. We investigate background Martian atmospheres of 50 and 500 mbar CO_2 with varying abundances of H_2O and sulfur volatiles (H_2S and SO_2 mixing ratios of 10^{-3} to 10^{-6}). Results suggest that these sulfur volatile influxes, alone, could have been responsible for greenhouse warming up to 25 K above that caused by CO_2. Including additional water vapor feedback, this process could have raised the early surface temperature above the freezing point for brines and possibly allowed transient liquid water on the Martian surface. Each temperature rise was likely to have been short-lived, however, due to brief residence times for sulfur volatiles in an optically thin atmosphere.

Citation: Johnson, S. S., M. A. Mischna, T. L. Grove, and M. T. Zuber (2008), Sulfur-induced greenhouse warming on early Mars, *J. Geophys. Res.*, *113*, E08005, doi:10.1029/2007JE002962.

1. Introduction

[2] The present geology of Mars points to the existence of a thicker, warmer atmosphere in the past. Climate change is best evidenced by the early age and distribution of dendritic valley networks and interior channels within these valley networks as well as geologic indicators of much higher erosion rates in ancient Martian history, such as degraded Noachian age craters [*Fanale et al.*, 1992; *Catling*, 2008]. Some have postulated the existence of a large ocean in the Northern Plains [*Baker et al.*, 1991; *Clifford and Parker*, 2001]. Mars Orbiter Laser Altimeter data suggest that the innermost of two proposed shorelines forms an approximately equipotential surface [*Head et al.*, 1999], and *Perron et al.* [2007] propose that coupled with the resistance of Mars' elastic crust, true polar wander over the past 2 to 3 Ga can account for much of the shorelines' topographic variation. The smoothness of the lowlands also may be explained by fluvially transported sediments [*Aharonson et al.*, 1998]. Others suggest that more sporadic climate variations led only to ephemeral rivers and lakes, or simply near-surface groundwater with multiple recharge events [*Segura et al.*, 2002]. At the Opportunity landing site, the sedimentary and mineralogical features associated with a sulfate-rich stratigraphic section at least seven meters in thickness suggest that water was present episodically for at least thousands of years [*Knoll et al.*, 2005], with no less than four distinct recharge episodes [*McLennan et al.*, 2005]. Orbital data indicate that this geological unit, associated with aeolian and shallow water deposition, and likely to be late Noachian or early Hesperian in age, extends over several hundred thousand square kilometers and reaches up to 800 m in thickness [*Hynek et al.*, 2002; *Arvidson et al.*, 2003, 2005].

[3] An increasing body of evidence from recent Mars exploration missions suggests that sulfur chemistry may have played an important role on early Mars. Although the Martian atmosphere contains virtually no sulfur species at present (upper limit = 0.1 ppm), all soils observed by landed missions have duricrust with enhanced sulfate abundances of 3–10% sulfate [*Maguire*, 1977; *Settle*, 1979; *Owen*, 1992; *Squyres et al.*, 2004]. Sulfate abundances in outcrops have been detected at even higher levels. Mg sulfates are estimated to constitute up to the 30% of the Meridiani Planum landing site outcrop [*Wänke et al.*, 2001; *Feldman et al.*, 2004], and the OMEGA hyperspectral imager aboard Mars Express has identified kieserite, gypsum and polyhydrated sulfates on localized layered terrains that extend well beyond these landing sites [*Gendrin et al.*, 2005]. The visible/infrared spectrometer aboard Mars Reconnaissance Orbiter, Compact Reconnaissance Imaging Spectrometers for Mars (CRISM), has targeted many of these hydrated sulfate deposits for further analyses [*Roach et al.*, 2007; F. Poulet, manuscript in preparation, 2008]. Most sulfate-rich deposits correspond to freshly exhumed surfaces that can be dated to the Noachian and/or Hesperian epochs. The layered deposits where OMEGA sees evidence for hydrated sulfates occupy a few percent of the equatorial to midlatitude regions; these deposits are on the order of a few hundred

[1] Department of Earth, Atmospheric and Planetary Science, Massachusetts Institute of Technology, Cambridge, Massachusetts, USA.
[2] Jet Propulsion Laboratory, California Institute of Technology, Pasadena, California, USA.

0148-0227/08/2007JE002962

meters thick, containing roughly 20 to 30 percent sulfate (R. E. Arvidson, personal communication, 2006).

[4] The SNC meteorites (shergottites, nakhilites and chassignites: basaltic, achondritic meteorites believed to have originated from Mars) contain sulfur, and isotopic sulfur data from the meteorites reflect deposition of sulfur species produced by atmospheric chemical reactions [*Farquhar et al.*, 2000]. Sulfur isotope measurements of oxidized and reduced sulfur reveal mass-independent fractionation, indicating that dynamic atmospheric chemistry has strongly contributed to the history of the Martian sulfur cycle and suggesting an important role for sulfur volatiles and sulfate aerosols in Martian history [*Farquhar et al.*, 2000].

[5] Sulfur volatiles, in the form of SO_2 and H_2S, act as powerful greenhouse gases and may have been important atmospheric components during periods of enhanced volcanic activity on Mars [*Postawko and Kuhn*, 1986; *Settle*, 1979]. Sulfur volatiles have also been suggested as serving a useful secondary role in warming early Mars; the presence of small amounts of SO_2 in the middle atmosphere may have kept temperatures warm enough to prevent CO_2 condensation, allowing for both a thicker CO_2 atmosphere and less reflectance of solar energy back to space [*Yung et al.*, 1997]. Without sulfur volatiles, many atmospheric models have struggled with two related problems: (1) creating the necessary warming for liquid water stability with CO_2 alone and (2) explaining the lack of carbonate deposition. Regarding the first problem, *Kasting* [1991] found that a dense early CO_2 atmosphere could not warm early Mars sufficiently to allow aqueous surface features without additional, complementary greenhouse gases, and *Postawko and Kuhn* [1986] found that even three bars of CO_2 would not provide sufficient warming to reach melting temperatures. Concerning the second problem, while carbonate platforms would be expected in abundance with a CO_2-rich atmosphere and an aqueous surface environment, none have been detected on the surface of the planet. Orbital Thermal Emission Spectrometer (TES) data constrain carbonate abundance in Martian dust to 1–2 wt % [*Bandfield*, 2002]. The discovery of the mineral jarosite, $(Na, K)Fe_3(SO_4)_2(OH)$, by Opportunity at Meridiani Planum indicates the presence of ancient acidic conditions on Mars, which could have prevented the deposition of carbonate, despite the fact that expected weathering reactions with widespread surface basalt layers would have served to buffer pH. This conclusion requires a source for surface acidity over Martian history.

[6] It has been proposed that outgassed sulfur species, and the subsequent formation of sulfuric acid aerosols in the atmosphere, may have been responsible for, among other things, (1) producing ubiquitous sulfur-rich dust and globally dispersed sulfate platforms, (2) creating the low pH levels of 2–4 that are suggested by the presence of jarosite, preventing carbonate deposition, and (3) generating relatively clement climatic conditions that allow for liquid water and brines at the surface of Mars via potent but short-lived greenhouse warming [see *Settle*, 1979; *Postawko and Kuhn*, 1986; *Blaney*, 1996; *Halevy et al.*, 2007]. A Martian history with significant sulfur outgassing may explain recent mission findings more comprehensively than theories in the literature which invoke (1) an extremely thick (multiple bar) CO_2 atmosphere [*Pollack et al.*, 1987; *Gulick et al.*, 1997], a CH_4-rich atmosphere [*Kasting*, 1997], or an NH_3-rich atmosphere with shielding by an organic haze layer [*Sagan and Chyba*, 1997] as the source of greenhouse warming; (2) near global coverage of scattering CO_2 ice clouds [*Forget and Pierrehumbert*, 1997; *Mischna et al.*, 2000]; (3) impacts as the source of heat for short-lived aquifer recharge [*Segura et al.*, 2002]; (4) weathering without the presence of liquid water at the rock-atmosphere interface over hundreds of millions of years as the source of surface evaporites [*Banin*, 2005]; (5) mechanical mixing of subsurface salts, brines and ices from large impact events as the source of the Burns Formation material in Meridiani Planum [*Burt et al.*, 2005]; or (6) aqueous oxidation of volcanic iron sulfides pyrite and pyrrhotite as the source of sulfate minerals [*Zolotov and Shock*, 2005]. What follows is the first model that has been created to account for both sulfur delivery to the early atmosphere of Mars and its subsequent atmospheric warming effects. We show in a feasibility demonstration that sulfur volatiles may have been key to warming the early Martian atmosphere.

2. Sulfur Solubility in Martian Mantle Melts

2.1. Batch Melting Model

[7] A batch melting model, in which decompression melting of the mantle takes place with the solid residue staying with the melt during most of its ascent, is used to assess the sulfur solubility in Martian silicate melts in equilibrium with metal sulfide. Regardless of ascent velocity and melt fraction volume, magma from mantle source regions in this model will arrive at the base of the lithospheric lid undersaturated in sulfur. This is due to the unique negative pressure dependence for sulfur solubility that dominates the positive temperature dependence in systems that contain FeO [*Holzheid and Grove*, 2002].

[8] At the base of the lithospheric lid, a final equilibration will take place before the liquid melt is advected to the planet's surface. While significant cooling in passage through the crust would affect the sulfur solubility limit (SSL), here we assume that chemical and thermal halo effects insulate the magma along cracks and in magma chambers.

[9] To calculate the SSL in liquid silicate conditions, *Mavrogenes and O'Neill* [1999] used the equation

$$\ln(\mathrm{SSL}) = \frac{A}{T} + B + C\left(\frac{P}{T}\right) + \ln a_{\mathrm{FeS}}^{\mathrm{sulfide}}, \quad (1)$$

where $a_{\mathrm{FeS}}^{\mathrm{sulfide}}$ is the activity of FeS in metallic sulfide and constants A, B, and C are derived from a fit to experimental data. The sulfur content in the silicate liquid is in ppm, temperature, T, in kelvin, and pressure, P, in bars. *Holzheid and Grove* [2002] adapted the equation from *Mavrogenes and O'Neill* [1999] by adding an additional parameter to assess the further dependence of sulfur solubility on the silicate liquid composition:

$$\ln(\mathrm{SSL}) = \frac{A}{T} + B + C\left(\frac{P}{T}\right) + D\ \mathrm{nbo}/t + \ln a_{\mathrm{FeS}}^{\mathrm{sulfide}}, \quad (2)$$

where nbo/t is the ratio of nonbridging oxygen anions to tetrahedrally coordinated cations in the silicate; it is a

measure of the degree of polymerization in the silicate melt structure. The value of $a_{FeS}^{sulfide}$ is taken to be ~1 as metallic sulfides are close to stoichiometric FeS in the experimental data [*Holzheid and Grove*, 2002].

[10] The empirically derived parameters (A, B, C, and D) are found by means of a nonlinear least squares regression of the sulfur solubility limits in liquid silicate from experimental data as a function of T (over the range 1573 to 1873 K), P (over the range 9 to 27 kbar) and nbo/t (over the range 0.46 to 1.62). These values in equation (2) are found to be −7714, 11.90, −0.038 and 0.368 for A, B, C, and D, with standard deviations of 2582, 1.65, 0.012 and 0.169, respectively [*Holzheid and Grove*, 2002].

2.2. Calculating Sulfur Solubility

[11] Alpha Particle X-ray Spectrometer (APXS) data from abraded, dark, vesicular basaltic rocks at the Spirit landing site in Gusev Crater are consistent with primitive basalts, with an average of 11 wt % MgO [*McSween et al.*, 2006]. Furthermore, laboratory experiments performed by *Monders et al.* [2007] on a basalt of a composition averaged from the unaltered Gusev basalts document a three-phase multiple saturation of olivine + orthopyroxene + spinel near the liquidus at 10 kbar and 1583 K. This result, at a point equivalent to a pressure depth of approximately 80 km, suggests the Gusev basalts either were generated or were last in equilibrium with mantle minerals not far below the approximately 50 km thick crust [*Zuber*, 2001].

[12] The primitive mantle compositions derived from the unaltered Gusev basalt composition are given in Table 1 for APXS targets Adirondack, Humphrey and Mazatzal. The compositional results were originally reported by *Gellert et al.* [2004], but the percentages in Table 1 reflect corrections made subsequent to new instrument calibrations completed in early 2005 [*McSween et al.*, 2006].

[13] We calculate an average value for nbo/t by using equations (3), (4), and (5) [*Mills*, 1993; *Mysen*, 1988]:

$$Y_{NB} = \sum \left[\begin{array}{l} x(SiO_2) + x(TiO_2) + x(Al_2O_3) + x(Cr_2O_3) \\ +x(FeO) + x(MnO) + x(MgO) + x(CaO) \end{array} \right], \quad (3)$$

$$X_T = \sum \left[\frac{x(SiO_2)}{2} + \frac{x(Al_2O_3)}{1.5} \right], \quad (4)$$

$$\mathrm{nbo}/t = \left(\frac{1}{X_T} \right) (2Y_{NB} - 4X_T), \quad (5)$$

where x is the mole fraction of the respective constituent.

[14] The resulting nbo/t value, 1.26, can be substituted into equation (2) along with the previously listed constants for A, B, C, and D, and T = 1583 K and P = 10 kbar. The resulting sulfur solubility at the 80 km depth equilibration region, as suggested by the *Monders et al.* [2007] experiments, is 1407 ppm.

[15] The 15 kbar anhydrous partial melting experiments of *Bertka and Holloway* [1994] at 1633 K on an iron-rich spinel lherzolite also simulated a Martian mantle composition as inferred from *Dreibus and Wanke* [1985]. Parallel calculations result in a broadly similar sulfur solubility of 1699 ppm. In addition, a number of effects not considered here may also serve to increase the release of sulfur volatiles and associated warming effects. Preliminary petrologic experiments suggest that the addition of a few weight percent of water to the melt could increase sulfur solubility by up to 50% (T. L. Grove, unpublished data, 2007).

Table 1. Extrapolated Rock End-Member Chemical Compositions for the Gusev Basalts

Oxides (wt %)	Adirondack	Humphrey	Mazatzal
SiO_2	45.30	45.85	45.55
TiO_2	0.49	0.58	0.57
Al_2O_3	10.42	10.40	10.72
Fe_2O_3	3.63	3.36	2.11
Cr_2O_3	0.62	0.67	0.59
FeO	15.71	15.67	16.83
MnO	0.42	0.42	0.43
MgO	11.90	10.67	10.34
CaO	7.76	8.15	8.23
Na_2O	2.09	2.35	2.62
K_2O	0.03	0.09	0.11
P_2O_5	0.54	0.59	0.63
FeS	0.83	0.83	0.83
Total	99.81	99.79	99.63

[16] The melting of metal sulfide, forming immiscible blebs of FeS, occurs approximately 400 K below the beginning of melting of the silicate mantle. Because the negative pressure dependence of sulfur solubility is more significant than its positive temperature dependence, adiabatic ascent will lead to sulfur undersaturation of a formerly sulfur-saturated magma [*Holzheid and Grove*, 2002]. When decompression melting commences in the batch-melting model, sulfur from these immiscible metal sulfide blebs will begin, and continue, dissolving directly into the silicate melt. The remaining metal sulfide will largely be left behind as the final equilibration takes place and melt is extracted at the base of the lithospheric lid. As surface temperature and pressure conditions are well beneath the vapor saturation pressures for both H_2S and SO_2 [*Lemmon et al.*, 2005], we assume that all 1407 ppm of soluble sulfur are released from the magma directly to the atmosphere. With an estimate for the sulfur concentration in Martian magma, we proceed now to estimate the sulfur volatile amounts potentially released by volcanic degassing.

3. Volcanic Release of Sulfur Volatiles

[17] The Tharsis igneous province is estimated to contain 3×10^8 km^3 of solidified magma. Volatile degassing associated with the formation, thought to be largely complete by the end of the Noachian, certainly affected the early Martian climate [*Phillips et al.*, 2001], yet it remains unclear to what extent the more deeply intruded magma in the Tharsis province may have communicated with the surface. Had magma been emplaced uniformly at a continuous rate, the impact of the sulfur species in the atmosphere is less likely to have had significant implications for warming over the late Noachian. Some abrupt, catastrophic volcanism events, however, are consistent with the current understanding of the surface geomorphology on Mars. For these reasons, we explore the consequences of sulfur volatiles on climate following large, discrete volcanic events associ-

Table 2. Prescribed Mixing Ratios and Partial Pressures[a]

	50 mbar	500 mbar
Mixing ratios		
SO_2	$6.14 \times 10^{-5}/2.45 \times 10^{-3}$	$6.14 \times 10^{-6}/2.45 \times 10^{-4}$
H_2S	$3.26 \times 10^{-5}/1.30 \times 10^{-3}$	$3.26 \times 10^{-6}/1.30 \times 10^{-4}$
Partial pressures (bars)		
SO_2	$2.11 \times 10^{-6}/8.40 \times 10^{-5}$	$2.11 \times 10^{-6}/8.40 \times 10^{-5}$
H_2S	$2.11 \times 10^{-6}/8.40 \times 10^{-5}$	$2.11 \times 10^{-6}/8.40 \times 10^{-5}$

[a]Format of each entry is Andrews-Hanna (lower bound)/Wilson (upper bound).

ated with dike emplacement features as interpreted by orbital reconnaissance.

[18] Analyzing near-surface dike intrusions associated with Tharsis radial graben, *Wilson and Head* [2002] estimate that a single giant dike intruded radial to a Tharsis volcano could inject up to 60,000 km^3 of magma over a timescale on the order of days. Under a different set of assumptions, *Hanna and Phillips* [2006] and J. C. Andrews-Hanna (personal communication, 2007) suggest a minimum emplacement volume of 1500 km^3 associated with some of these features. We examine volatile pulses associated with both a lower bound "Andrews-Hanna" model and an upper bound "Wilson" model. For the purposes of our model, we assume that sulfur volatile release occurs within the first few weeks of the simulation. Although the majority of this volcanism is intrusive, gases are thought to segregate up to the top of these dikes forming collapse craters and/or creating the necessary pressure to generate explosive eruptions, as was likely in the Memnonia Fossa region [*Scott et al.*, 2002]. Convective overturn in wide dikes (>100 m) is also thought to enhance this process of rapid volatile release. It is important to note that there would have certainly been flood basalt eruptions of similar magnitudes, presumably also driven by mantle plumes, on early Mars. We focus on giant dike swarm formation as it allows us estimate with more specificity the total magma emplacement in a single event. It is interesting to note that *Thordarson and Self* [2003] found that the largest lava flow in recorded history, the 1783–1784 flood basalt eruption associated with the Laki volcanic fissure in Iceland, released 15 km^3 of basalt and 122 megatons of SO_2 into the atmosphere over a period of 8 months, with nearly half released in the first 6 days. This proportion of sulfur release is within a factor of 2 of our estimate for Mars.

[19] The density of the Gusev basalt magma is calculated to be 2820 kg/m^3 [*Greeley et al.*, 2005], using the method of *Bottinga and Weill* [1970] with the parameters of *Mo et al.* [1982]. In our atmospheric calculations, we consider the range of exsolved volatiles associated with a pulse of 1500 km^3 to 60,000 km^3 of magma emplacement: 1.19×10^{13} to 4.76×10^{14} kg of SO_2 or 6.32×10^{12} to 2.53×10^{14} kg H_2S. These correspond to the mixing ratios listed in Table 2.

[20] We examine both SO_2 and H_2S end-members in our simulations of greenhouse warming. Analysis of shergottite meteorite data suggests that the mantle source of Martian basalts had a redox state within one log unit of the iron-wüstite buffer [*Wadhwa*, 2001]. As the magma may remain buffered by the mineral assemblages through its ascent to the surface, part of the sulfur could have been released to the atmosphere with an oxidation state of −2, forming H_2S. Yet, SO_2 is a likely intermediate in the process of sulfur volatile removal from the atmosphere, with reaction rates for liberated O and OH radicals in the pathway from H_2S to SO_2 (via HS and HSO or HS and SO) exceeding those in the pathway from SO_2 to sulfate (via SO_3) [*DeMore et al.*, 1997]. Although it should be noted that SO_2 disproportionation reactions are also possible, generating elemental sulfur and sulfate as products of atmospheric photochemistry [*Zahnle and Haberle*, 2006], our investigation primarily explores the exclusive volatile form of SO_2. At the beginning of the simulations, we assume either gas (H_2S or SO_2) to be uniformly mixed in the atmosphere.

4. Atmospheric Warming

4.1. General Circulation Model

[21] We use the Mars Weather Research and Forecasting (MarsWRF) general circulation model (GCM) as the basis for our atmospheric warming experiments [*Richardson et al.*, 2007]. The MarsWRF GCM solves the primitive equations using a finite difference model on an Arakawa-C grid, and is run with a latitude by longitude model resolution of 5° × 5.625° (36 × 64 grid points) and with 25 vertical levels on a modified sigma (terrain-following) vertical coordinate. The total present-day atmospheric CO_2 budget has been tuned to fit the Viking Lander annual pressure curves. We then scale the present-day annual and global average surface pressure (~6 mbar) to either 50 or 500 mbar, depending on the scenario being considered. Both surface albedo and thermal inertia are matched to present-day TES observations [*Christensen et al.*, 2001; *Putzig et al.*, 2005], and the present-day topography is used. Tests of the MarsWRF dynamical core [*Richardson et al.*, 2007] show that it produces results that compare favorably to the Held-Suarez "standard" [*Held and Suarez*, 1994] under terrestrial atmospheric conditions. Comparisons to existing Mars climate models and vertical profiles of TES data further show that MarsWRF is able to replicate key features of the Martian atmosphere quite well. At the Second International Workshop on Mars Atmosphere Modeling and Observations in Granada, Spain, in March 2006, a broad model intercomparison was performed between seven independent Mars GCMs, including MarsWRF, to study their ability to reproduce observations of the Martian atmosphere. Sample results from this (unpublished) intercomparison are shown in Figure 1. In each of the four comparisons, output from MarsWRF for its "best fit" to present-day temperature and zonal wind profiles is shown alongside the same field for both the GFDL Mars GCM [*Wilson and Hamilton*, 1996] and LMD/AOPP Mars GCM [*Forget et al.*, 1999]. For all four comparisons, atmospheric dust is set to a column opacity of 0.2. The intercomparison results are quite good at both solstice seasons, as well as during the equinoctial periods (not shown), and capture the winter zonal jets both in magnitude and location, as well as the zonal temperature gradient across the planet. Small differences between the simulations are due largely to differences in model architecture (i.e., different dynamical cores). These preliminary results provide confidence in the behavior of MarsWRF. Additional comparisons to TES temperature data [*Smith et al.*, 2001] further show a high

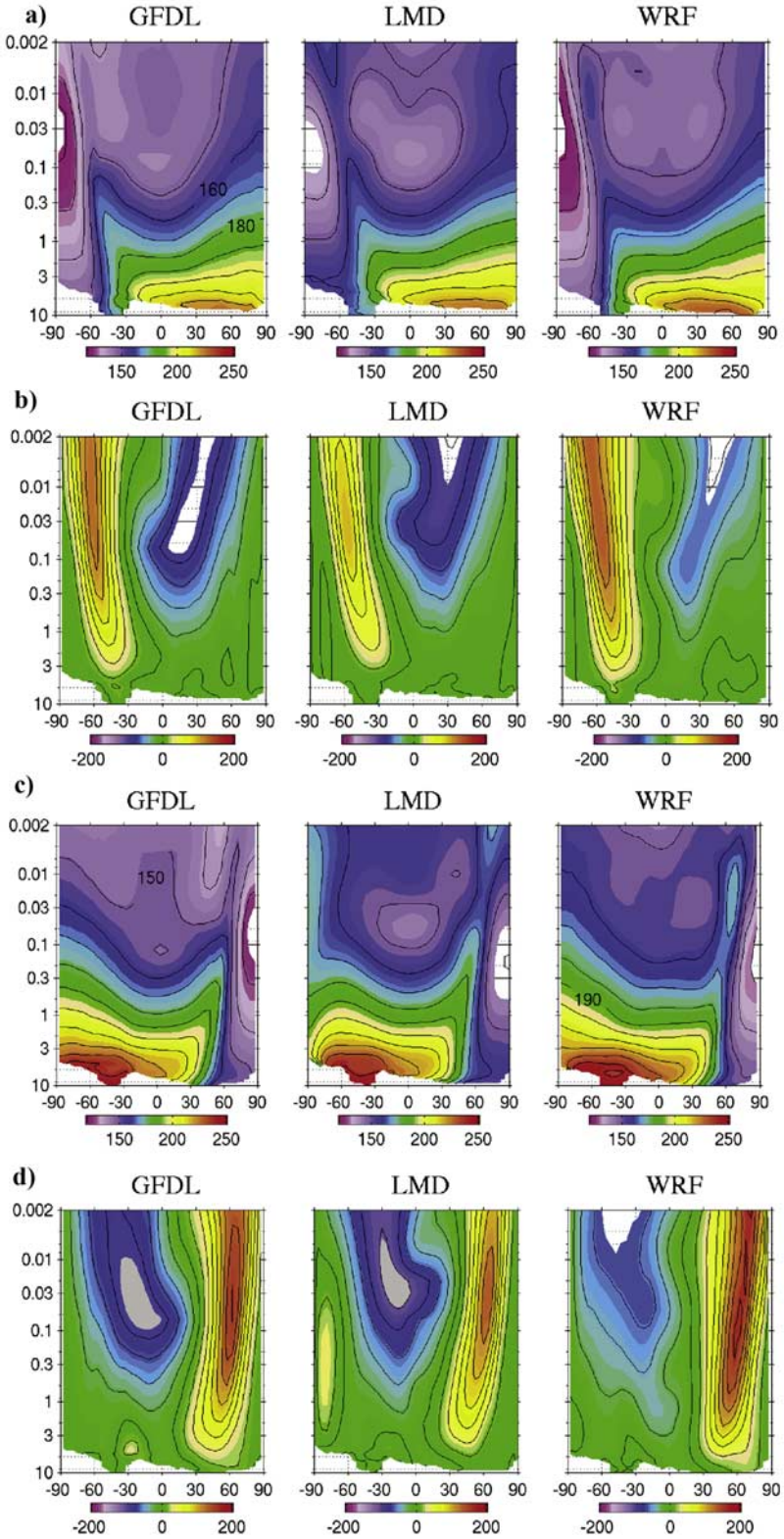

Figure 1. Comparison of MarsWRF output to model output from the GFDL Mars GCM and the LMD/AOPP Mars GCM. (a) Zonal mean temperature for $L_s = 90°$, (b) zonal mean zonal wind for $L_s = 90°$, (c) same as Figure 1a but at $L_s = 270°$, (d) same as Figure 1b but at $L_s = 270°$. All models have $\tau = 0.2$ column dust opacity. Ordinate units are millibars.

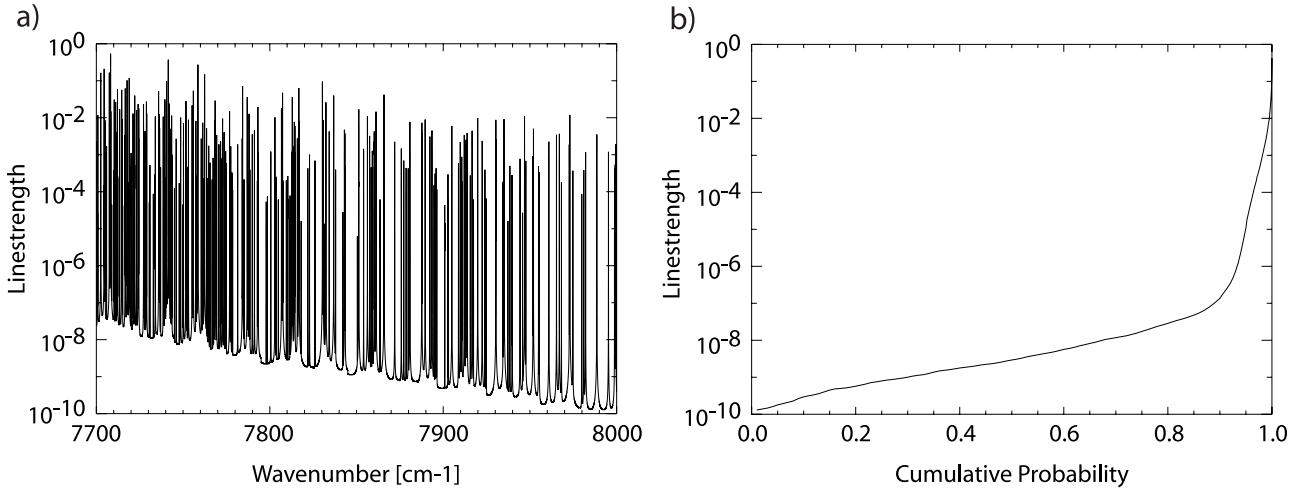

Figure 2. Comparison of a portion of the CO_2 spectrum both (a) unsorted and (b) sorted by strength as a k distribution. The sorted spectrum is substantially smoother than the unsorted spectrum, and the curve can be well approximated by few points. The elbow in the sorted curve marks the beginning of the contribution of the strong line cores in the distribution versus the relatively weaker line wings.

degree of similarity to observations [*Richardson et al.*, 2007].

4.2. Radiation Scheme

[22] We have developed a new multigas, two-stream radiation code loosely based on the structure of the UK Hadley Centre Radiation Scheme [*Edwards and Slingo*, 1996], but modified to use the k distribution radiative transfer method. This method retains much of the accuracy of line-by-line calculations, but is significantly faster, making it ideal for computationally expensive 3-D global models. Details about the k distribution method can be widely found [e.g., *Lacis and Oinas*, 1991; *Fu and Liou*, 1992], so only a brief summary of relevant points will be provided here.

[23] The numerical scheme regarding the k distribution method involves partitioning the solar/IR spectrum into distinct spectral bands, and re-sorting the individual lines, which are highly variable as a function of wavelength, within each band to produce a relatively smooth curve that is more conducive to numerical approximation. Each distinct band is both sufficiently narrow such that the Planck blackbody curve is approximately constant across the entire band and also sufficiently broad to encompass full absorption features of individual gases. In the present implementation of this k distribution method, the entire solar/IR spectrum is partitioned into 12 bands (seven solar, five IR) of varying widths, following the partitioning employed by the Ames MGCM (versions 2.0 and greater) (R. M. Haberle, personal communication, 2007). Errors introduced by variations in the Planck function across these spectral bands are quite nominal [*Haberle et al.*, 2003]. Bands are prudently selected to ensure that individual absorption features are not bisected across two bands. Once band sizes are selected, the portion of the spectrum within each band is discretized at a subline width frequency, and these discrete intensities are sorted by magnitude. A before-and-after illustration of this type of line sorting is shown in Figure 2. The sorted curve in Figure 2b no longer maps line intensity directly to wavelength, but instead maps intensity to a cumulative probability function, i.e., what fraction of the intensities are smaller than the given intensity.

[24] For a standard line-by-line calculation, the transmissivity, Tr, is calculated as

$$Tr = \int_{\nu_{\min}}^{\nu_{\max}} \exp[-k_\nu u] d\nu, \tag{6}$$

where k_ν is the absorption coefficient at frequency ν, and u is the mass of the absorbing gas. Following the resorting of this spectrum, transmissivity is calculated as

$$Tr = \int_0^1 \exp\left[-k_g u\right] dg, \tag{7}$$

where now k_g is the absorption coefficient for the cumulative probability g (between zero and one).

[25] Within each band, we perform the discretization and sorting to develop a smooth cumulative probability curve. We then fit this curve with 16 quadrature points at specified intervals along the distribution: eight points in the lowest 95% of the distribution and eight points in the upper 5%. These intervals were selected because experimentation has shown that the strongest absorption, which occurs at the cores of individual spectral lines, takes place in the top 5% of the distribution, so extra precision is warranted. From this, we can obtain a numerical approximation to the transmissivity for a given atmospheric layer of mass u

$$Tr = \sum_{i=1}^{16} a_i e^{-k_i u}, \tag{8}$$

where k_i is the absorption coefficient chosen at quadrature point i, and a_i is the assigned weight (where $\Sigma\, a_i = 1$).

[26] Absorption coefficients vary according to both temperature and pressure. To maintain the best accuracy possible in our absorption calculations, we have assembled, offline, a series of databases containing the k distribution absorption coefficients for the full range of p, T conditions expected in the atmospheres used for this study (T = 50–400 K in 1 K increments; $p = 10^{-4}$–10^{6} Pa with log(p) spacing of 0.2). The most basic database is for a pure CO_2 atmosphere. Here, and in all other databases in this study, the CO_2 mixing ratio is fixed at 0.953. Spectral line data are obtained from the HITRAN database [*Rothman et al.*, 2005] and internal partition sum data of *Fischer et al.* [2003]. The Humlícek approximation to a Voigt line shape is used to obtain the pressure and temperature-dependent line shape [*Humlícek*, 1982]. A second database was assembled for a dual-gas (CO_2 + H_2O) atmosphere over the same pressure/temperature conditions as above, but also across a range of putative water vapor mixing ratios (q, where $q = 10^{-7}$ to 10^{-2} by decade). The water vapor foreign continuum, which represents the net contribution of the distant tails of water vapor absorption lines, is parameterized (E, Mlawer et al., manuscript in preparation, 2008) and included in this and any other databases containing water.

[27] Two databases were assembled for each of the two-gas mixtures (SO_2 + CO_2) and (H_2S + CO_2), at both the upper and lower bound values of the sulfur species. Rather than calculating k coefficient data over a range of SO_2 or H_2S mixing ratios as was done for H_2O, we use the fixed sulfur species abundances found in Table 2 to build the database. This reduces the overall size of the database, and simplifies its construction, but also reduces the relevant parameter space to only those atmospheres with these precise sulfur species mixing ratios. For an investigation such as this, where specific atmospheric compositions are being considered, such an approach is acceptable. Last, a series of databases were assembled for all three-gas (SO_2/H_2S + CO_2 + H_2O) permutations, covering the same parameter space as the others. In total, 16 databases were required for the present study.

[28] To assemble a database, the raw (unsorted) spectra are calculated for each p, T, q triad and then partitioned into 12 spectral bands where they are discretized and sorted by strength as noted above. Within each of the 12 bands and for each p, T, q combination, the 16 k coefficients are obtained from the smoothed spectral curve and stored in the database (for a total of ~20 million coefficients per database). The weighting function for the k coefficients is the same for all bands, and for all p, T, q triads.

[29] These k coefficient databases are then used by the two-stream radiation code as lookup tables, from which the appropriate k coefficients are obtained for the specific p, T, q conditions at each model grid point, using the nearest neighbor in temperature and a linear interpolation in log space for both p and q. The corresponding radiative calculations are then performed to determine atmospheric heating rates. While such a process is, somewhat slower than current methods [e.g., *Hourdin*, 1992; *Forget et al.*, 1999], it is not unduly so. Because the k coefficient databases are calculated directly from the HITRAN database, we are able to choose at the outset any arbitrary combination of atmospheric species to investigate and convolve their respective spectra into a single distribution, thus this method is not only very useful for investigating atmospheres with varying compositions but also generic enough to be used on virtually any planet with an atmosphere. Currently, implementations of this code are being developed for the atmospheres of Titan and Venus.

[30] Other radiation schemes commonly used for the Martian atmosphere have two major drawbacks that prevent their application to the present study. First, they are designed to best represent the present Martian climate, and are thus designed for compositionally pure CO_2 model atmospheres (since H_2O is radiatively negligible in the current Martian atmosphere). Second, they are tuned for atmospheres having surface pressures similar to present-day (6–10 mbar) and not for thick atmospheres. Above ~100 mbar, for example, the model of *Hourdin* [1992] has been shown to become increasingly unreliable, making it impossible to investigate the model atmospheres we present here.

4.3. Water Cycle

[31] The model is initialized with a globally uniform 10^{-6} water vapor mixing ratio and is free to evolve without additional external adjustments. The MarsWRF water cycle provides a simple mechanism for the transport, sedimentation, and exchange of water between the vapor and ice phases. For each model time step, both water vapor and water ice (treated independently in the model) are advected by the local wind field and diffused down the local vapor/ice gradient. At the conclusion of each model time step, the ice sediments at a pressure-dependent velocity according to the Stokes-Cunningham slip-flow equation [*Conrath*, 1975; *Haberle et al.*, 1982], assuming uniform 10 μm radius particles.

[32] The primary source of water for the atmosphere is from surface ice. Exchange of water vapor with the surface in MarsWRF follows the classical equation of *Flasar and Goody* [1976] and used by *Montmessin et al.* [2004] [*Forget et al.*, 1999]:

$$F_w = \rho C_d u_* (q_{sat} - q_v), \tag{9}$$

where u_* is the friction velocity, set to the horizontal wind in the lowest model layer, q_{sat} is the water vapor saturation mixing ratio at the surface temperature, and q_v is the local atmosphere water vapor mixing ratio. The resulting flux determines the magnitude of vapor flowing into/out of the atmosphere, and is proportional to the difference in humidity between the surface and atmosphere.

4.4. Dust and Solar Luminosity

[33] For present-day conditions, MarsWRF generally uses a time- and space-varying dust distribution modeled on MGS observations [*Montmessin et al.*, 2004], but test cases have been run with no dust, or with a fixed global abundance. It is not evident whether any of these specific distributions can be translated to higher pressure regimes with any physical basis. For this reason, radiatively active dust was excluded in the present simulations, though the presence of atmospheric dust would likely cause additional warming in our model. Future investigations may gauge the impact of a simplified dust scheme on the dynamics of the system. The incoming solar luminosity is chosen to be conservative: 75% of the modern value, as has been

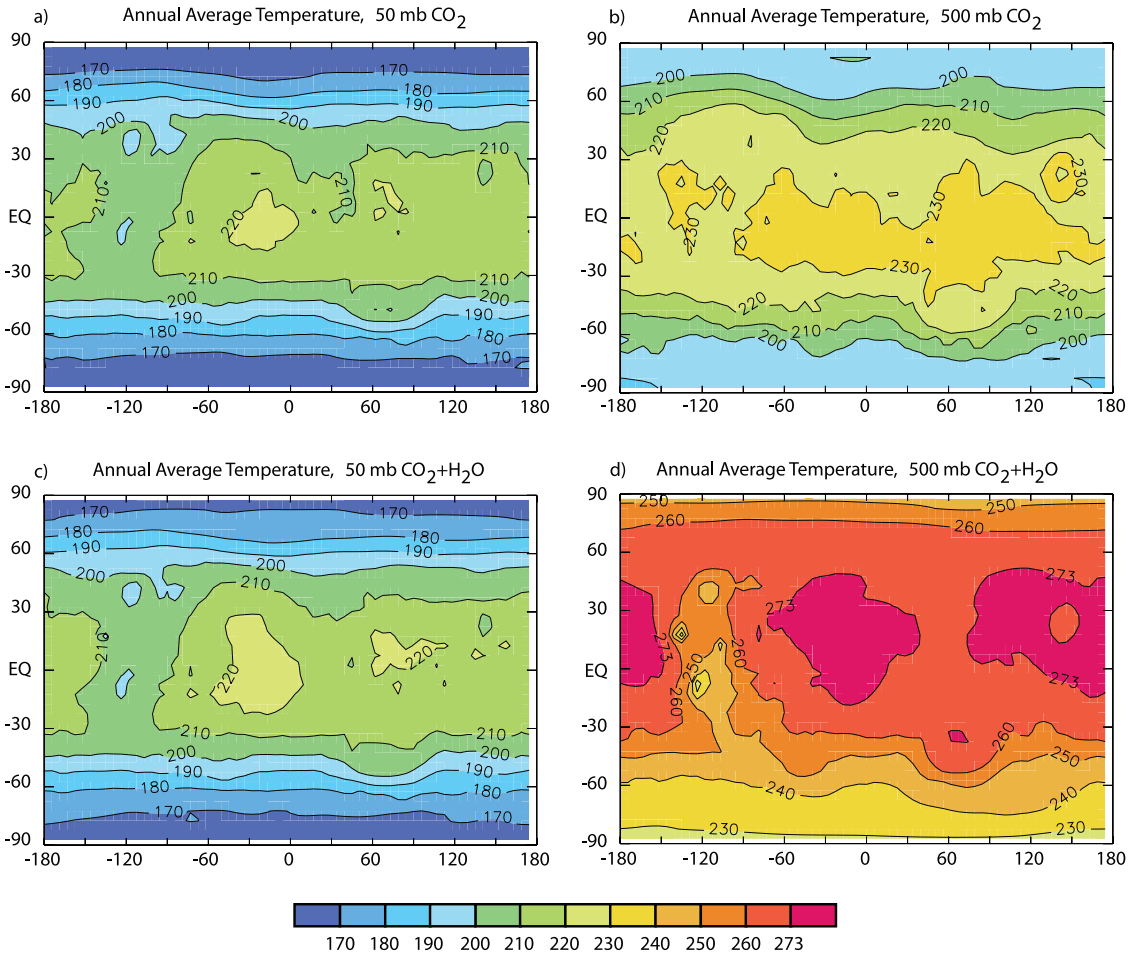

Figure 3. Annual average surface temperatures (in kelvin) for control simulations: (a) 50 mbar atmosphere, CO_2 only, (b) 500 mbar atmosphere, CO_2 only, (c) 50 mbar atmosphere with CO_2 + H_2O, and (d) 500 mbar atmosphere with CO_2 + H_2O.

traditionally demanded by solar evolution models [*Gough*, 1981].

5. Results

[34] Water vapor and the sulfur species each contribute a fraction of the total greenhouse warming in the system (above that generated by CO_2 itself). To identify the magnitude of warming produced by water vapor alone, we have run a series of "control" simulations at both surface pressures to quantify the effect of water vapor in the atmosphere. Results from all simulations in this work are shown for the third year, when the atmospheric vapor distribution has reached an approximate steady state. Figures 3a and 3b show annually averaged surface temperatures at 50 mbar and 500 mbar CO_2, respectively, without water vapor. Figures 3c and 3d show their water vapor-inclusive counterparts. The temperature difference between Figures 3a and 3c shows the warming contribution of water vapor. At 50 mbar (Figures 3a and 3c), water vapor plays only a minor role in atmospheric warming, generally enhancing temperatures by <5 K. There is little water vapor in this atmosphere due to low (<170 K) surface temperatures in the polar regions (particularly the north polar region where the residual water ice cap resides). Vapor flux is highly sluggish at the temperatures.

[35] In contrast, polar temperatures are substantially warmer in the 500 mbar scenario, and polar ice sublimation is more vigorous. During summer, when nearly all sublimation occurs, the disparity between the two pressure scenarios is significant. Annual maximum temperatures at the North Pole at 50 mbar rise to only 170 K, while at 500 mbar, annual maxima approach 230 K. The vapor holding capacity is a factor of 10,000 greater at the polar temperatures in the 500 mbar simulation, permitting a vastly greater quantity of vapor to flow into the atmosphere. Additionally, the larger thermal inertia of the thicker atmosphere prevents nighttime temperatures from dipping to the low values in the 50 mbar simulation, allowing a greater amount of water to remain in the atmosphere. The end result of this greater vapor content at 500 mbar is a surface that is ~40 K warmer than its water-free counterpart, including some tropical locations with mean temperatures above the water ice melting point (Figure 3d).

[36] It should be noted that the present implementation of MarsWRF does not account for the radiative effects of water

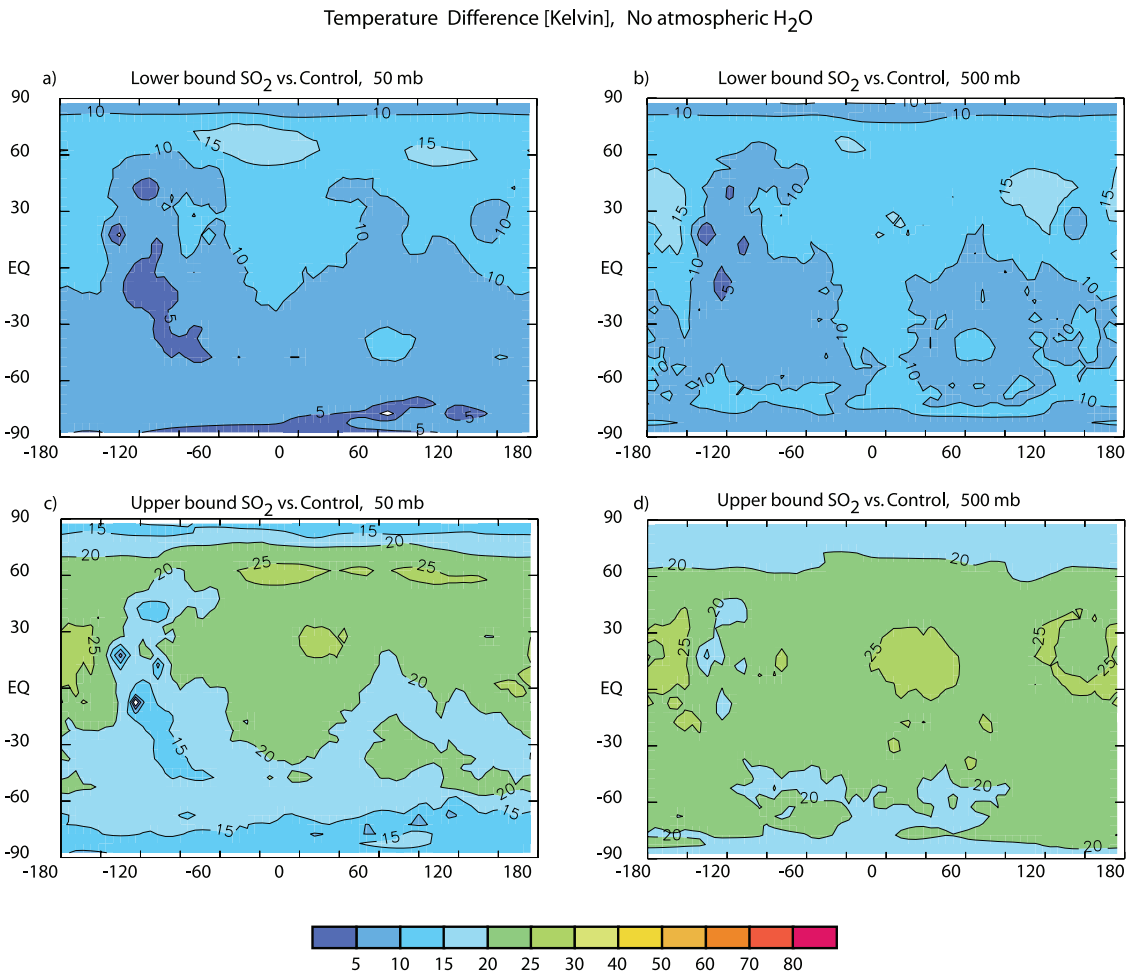

Figure 4. Difference (in kelvin) in annual average surface temperature between the "dry" control simulations and SO_2 pulse simulations, without the effects of water vapor included, illustrating the magnitude of warming from SO_2 alone. (a) Lower bound SO_2 abundance in 50 mbar atmosphere, (b) lower bound SO_2 abundance in 500 mbar atmosphere, (c) upper bound SO_2 abundance in 50 mbar atmosphere, and (d) upper bound SO_2 abundance in 500 mbar atmosphere. "Control" simulation for Figures 4a and 4c is that in Figure 3a and for Figures 4b and 4d is that in Figure 3b.

ice clouds, which are believed to have an overall cooling effect. In these humid atmospheres, thick, low (and bright) convective clouds will likely be present, raising the planetary albedo, reducing the amount of insolation at the surface, and lowering surface temperatures. We do not consider this negative radiative feedback cycle at present in MarsWRF (although we do model the opacity and distribution of water ice clouds), thus the temperature results may be upper limits depending on the abundance of clouds and their specific distribution both horizontally and vertically.

[37] In parallel with the Figure 3 depiction of the extent of greenhouse warming by H_2O, Figure 4 shows the warming by "Wilson" upper and "Andrews-Hanna" lower bound amounts of SO_2 in a dry (no H_2O) CO_2 atmosphere. For the 50 mbar "Andrews-Hanna" lower bound atmosphere, annual average warming by SO_2 is generally of the order of 7–15 K (Figure 4a), while for the "Wilson" upper bound, this warming increases to 15–25 K (Figure 4c). There is a noticeable hemispheric dichotomy present in both panels, mirroring the lower altitude and greater atmospheric mass present in the north. For a fixed SO_2 mixing ratio, there is more SO_2 present in an overhead column in the Northern Lowlands, and hence more greenhouse warming. The magnitude of warming introduced by the presence of SO_2 in the atmosphere is in line with the estimates of *Postawko and Kuhn* [1986]. Simulations involving H_2S show it is a less efficient greenhouse gas than SO_2. The results of these simulations are shown in Table 3.

[38] In the 500 mbar scenario, there is approximately the same level of warming as in the 50 mbar scenarios, which is expected. The magnitude of greenhouse warming is largely a consequence of the mass of the species, as opposed to its mixing ratio. In both scenarios, the atmospheres have the same total mass of SO_2, and hence have similar greenhouse effects. The magnitude of warming is slightly greater in the 500 mbar scenario. This small increase is a consequence of greater absorption caused by increased pressure broadening of the spectral lines in the thicker 500 mbar atmosphere.

Table 3. Sensitivity Analysis for Warming Results[a]

	Average T (K)	Max > 260 K (%)	Max > 273 K (%)	Max ΔT[b] (K)
50 mbar without water				
SO_2 upper bound	214	35	29	27
SO_2 lower bound	204	21	12	18
H_2S upper bound	198	17	9	9
H_2S lower bound	196	16	9	5
Control (“dry”)	195	16	9	–
50 mbar with water				
SO_2 upper bound	225	48	38	43
SO_2 lower bound	208	25	14	21
H_2S upper bound	199	18	10	7
H_2S lower bound	198	17	10	5
Control (“wet”)	197	16	9	–
500 mbar without water				
SO_2 upper bound	237	53	32	27
SO_2 lower bound	226	30	12	17
H_2S upper bound	232	36	18	29
H_2S lower bound	219	17	9	10
Control (“dry”)	215	16	8	–
500 mbar with water				
SO_2 upper bound	315	100	100	70
SO_2 lower bound	283	100	100	31
H_2S upper bound	264	100	99	9
H_2S lower bound	259	100	89	1
Control (“wet”)	258	100	87	–

[a]Average temperatures are global, annual average surface temperatures. Max > 260 K shows the fraction of the year for which the warmest surface location has a surface temperature >260 K (a reasonable brine freezing point). Max > 273 K is the same but for the pure water freezing point. Max ΔT shows the maximum temperature deviation of the warmest surface location from the same point in the control run.

[b]Versus control run for matching pressure/water vapor configuration.

[39] Figure 5 shows the result of combining both H_2O and SO_2 greenhouse warming in each of our two pressure scenarios. In Figure 5, the “control” scenario is “wet” and contains both CO_2 + H_2O (compare Figures 3c and 3d). This is different from Figure 4, where the “control” is “dry” (compare Figures 3a and 3b). In each of the four scenarios presented in Figure 5, the same amount of SO_2 is present in the atmosphere as for the respective scenarios in Figure 4; thus, at first guess, one might assume the same level of warming (i.e., 7–25 K) by SO_2 here, above the “wet” control run, as in Figure 4 above the “dry” control run. Instead, we find the temperature differences in Figure 5 to be not only larger than in Figure 4, but also increasingly large as we move from “Andrews-Hanna” lower to “Wilson” upper bound values and from 50 to 500 mbar (e.g., Figure 5a shows only slightly more warming than Figure 4a, while Figure 5d shows substantially more warming than Figure 4d). Since this added warming is not produced by the SO_2 or CO_2, both of which have fixed abundances, it must be obtained from atmospheric water vapor. This is a clear demonstration of the positive feedback between SO_2 and H_2O greenhouse warming in the atmosphere. The addition of SO_2 provides a “boost” in temperature, permitting even more water vapor into the atmosphere, further augmenting the already significant greenhouse effect. In the “Wilson” upper bound SO_2 500 mbar case, this corresponds to additional warming by H_2O vapor of 25 K. For cooler scenarios, or those with a smaller SO_2 “boost,” the additional H_2O increase is correspondingly less.

[40] An underlying objective of this work is to explore regions on the surface where enhanced greenhouse warming may provide conditions for liquid water to be present at the surface. This requires satisfying both atmospheric pressure and temperature restrictions [*Richardson and Mischna*, 2005]. For these thick atmospheres, the pressure restriction is fully satisfied, which means that the potential for liquid water is constrained only by temperature. This temperature constraint is nominally 273 K, but may be several tens of degrees lower depending on the salinity of the water. Figure 6 maps the fraction of the year when temperatures at each surface location exceed the nominal liquid water melting temperature of 273 K under the listed atmospheric compositions, thus suggesting those places where the potential for liquid water would be greatest.

[41] At 50 mbar, much of the planet can sustain liquid for at least a portion of the year, Generally, between 1 and 30% of the year reaches temperatures >273 K, with these times occurring during the warmest periods: summertime, and in the midafternoon hours. The exception is the Northern Hemisphere, where summertime temperatures are colder, and over Tharsis when the SO_2 abundance is too low. This dichotomy is a direct result of the orbit chosen for this particular simulation, which is the same as present-day. For a different orbital configuration (e.g., if perihelion occurred during northern summer), summertime temperatures would be warmer in the north and cooler in the south, and the distribution would be different than shown in Figure 6, though the overall magnitudes would remain roughly the same. The situation is more favorable at 500 mbar, where a majority of the planet is >273 K for at least half of the year, and much of the planet is permanently above this value.

[42] Tying this all together, Figure 7 illustrates the maximum potential warming made possible by mixtures of SO_2 + H_2O above the baseline temperature of a “dry” CO_2 atmosphere. These magnitudes range from 10 to 20 K for “Andrews-Hanna” lower bound SO_2 at 50 mbar to over 100 K for the warmest, “Wilson” upper bound SO_2 at 500 mbar scenario. Once again, these values will not be typically obtained because of the negative feedbacks imposed by the water cycle itself. It is interesting, however, to note that the greatest warming occurs over the cold north polar cap where the summertime vapor concentration is the highest anywhere on the planet, and thus the potential for enhanced warming is greatest.

[43] Table 3 provides a summary of conditions found for each of the simulations run, including those in Figures 3–6. Additional surveys of global average temperatures, including those for H_2S, are listed, along with measures of frequency of time above 260 K (a nominal brine melting temperature) and 273 K and the magnitude of greenhouse warming introduced by sulfur volatiles and water vapor.

6. Discussion

[44] Our results suggest that volcanic release of sulfur volatiles in the early Martian atmosphere may have generated significant additional warming by trapping heat in wavelength-dependent atmospheric windows different from those of CO_2 and H_2O. Alone, SO_2 pulses may have generated up to 25 K of warming. In combination with water vapor feedbacks, surface temperatures after an SO_2

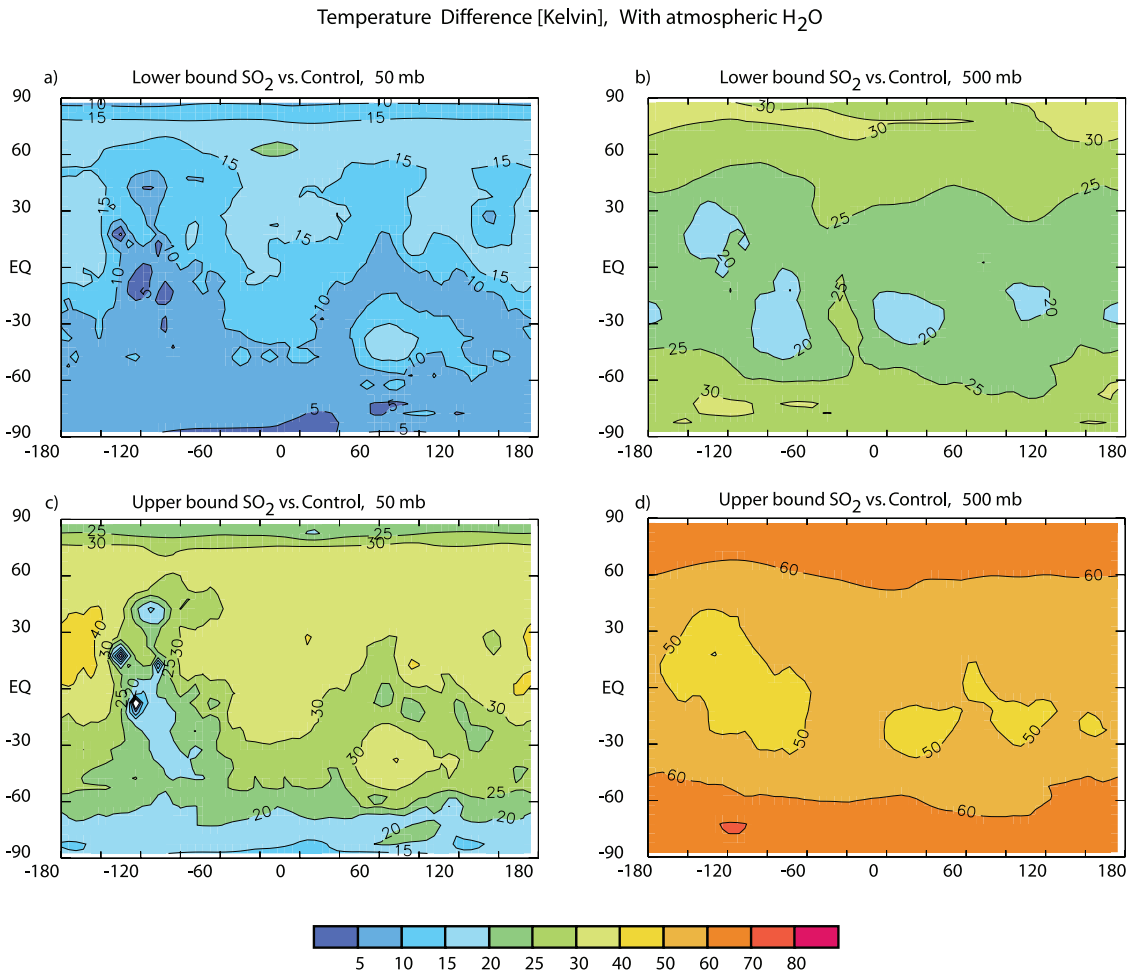

Figure 5. Difference (in kelvin) in annual average surface temperature between the "wet" control simulations and SO_2 pulse simulations, with the effects of water vapor, depicting the combined warming from SO_2 and water vapor feedbacks. (a) Lower bound SO_2 abundance in 50 mbar atmosphere, (b) lower bound SO_2 abundance in 500 mbar atmosphere, (c) upper bound SO_2 abundance in 50 mbar atmosphere, and (d) upper bound SO_2 abundance in 500 mbar atmosphere. "Control" simulation for Figures 5a and 5c is that in Figure 3c and for Figures 5b and 5d is that in Figure 3d.

pulse may have risen 50–70 K or more above a steady state CO_2 atmosphere, creating widespread surface conditions conducive to the presence of transient liquid water. Furthermore, as we have already noted, freezing points can be depressed by salt composition in brines [*Clark and Van Hart*, 1981]. Although the most logical choice of salt under these conditions, sulfate, is a poor freezing-point depressor, high levels of chlorine have been detected in soils at the landing sites for Spirit, Opportunity, Pathfinder and the Viking Landers, and salts may have been mobilized and concentrated by repeated wetting and evaporation events in ephemeral saline pans [*Yen et al.*, 2005; *Rutherford et al.*, 2001]. In his work on the stability of brines on Mars, *Brass* [1980] suggested a freezing point depression that easily allows for liquid phases within the upper range of our model results.

[45] The length of time that sulfur-related greenhouse warming persists in the atmosphere is a key area for additional work. Although sulfur volatiles are converted to sulfate aerosols within days in the Earth's current oxidizing atmosphere (often creating a global cooling effect following sulfur-rich volcanic eruptions, as in the 1991 eruption of Mount Pinatubo). A study of sulfur photochemistry in the current Martian regime reveals a 600-day lifetime for SO_2 [*Wong et al.*, 2004, 2005]. However, this lifetime will change significantly under the weakly reducing atmospheric conditions that likely characterized early Mars. We have begun photochemical modeling using an adaptation for Mars of a one-dimensional photochemical model developed for sulfur chemistry simulations in the Earth's Archean atmosphere [*Pavlov and Kasting*, 2002]. Our results suggest that the warming associated with these pulses is on the order of at least hundreds of years [*Johnson et al.*, 2007, also manuscript in preparation, 2008].

[46] Inputs of sulfur volatiles to the early Martian atmosphere are consistent with the evolution of early Mars proposed by *Bibring et al.* [2005, 2007], in which the planet experienced an early wet period of phyllosilicate formation followed by an arid, acidic period under which evaporitic sulfate deposits formed; this model invokes a surge in Tharsis outgassing near the end of the late Noachian to explain the transition from phyllosilicate to sulfate

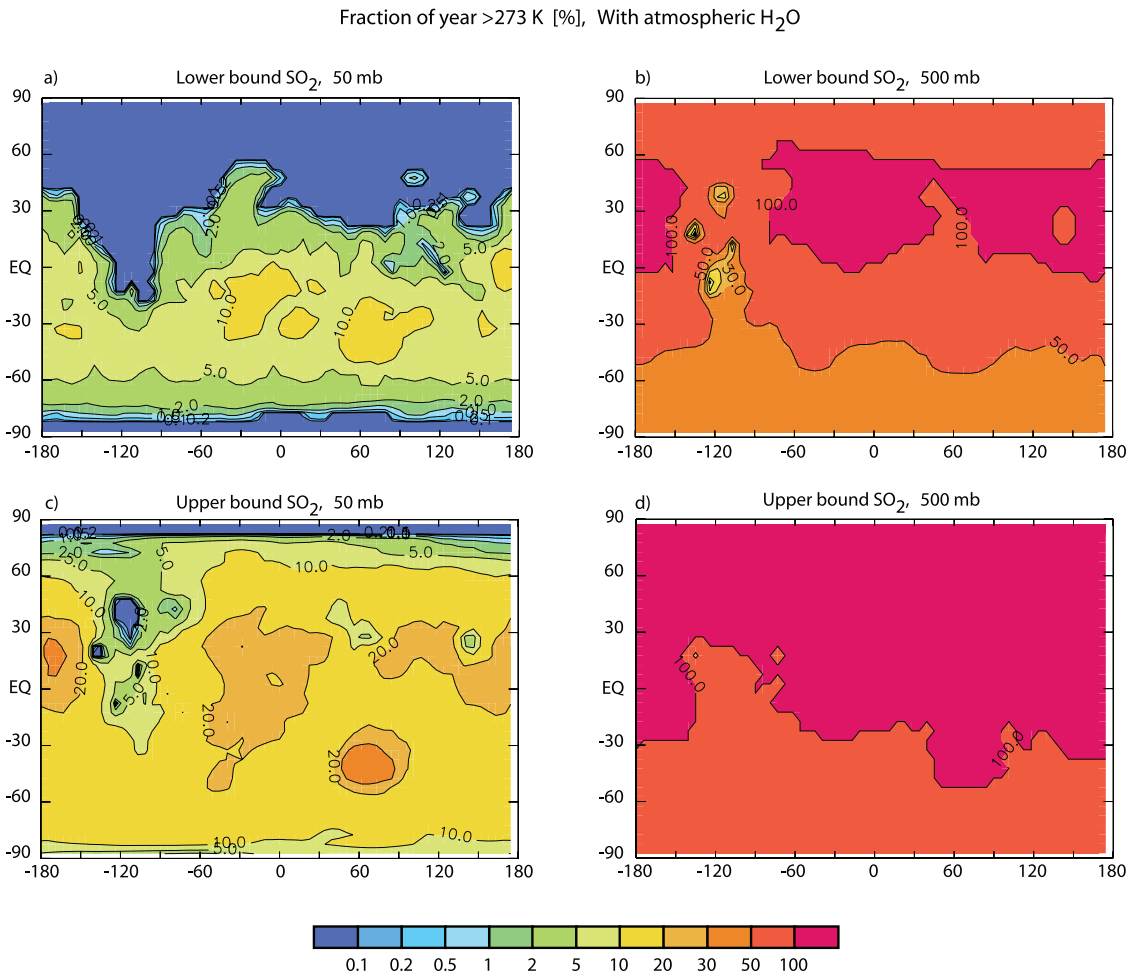

Figure 6. For the same configurations as Figure 5, fraction of the year (in percentage) that surface temperatures are >273 K at each model grid point. (a) Lower bound SO_2 abundance in 50 mbar atmosphere, (b) lower bound SO_2 abundance in 500 mbar atmosphere, (c) upper bound SO_2 abundance in 50 mbar atmosphere, and (d) upper bound SO_2 abundance in 500 mbar atmosphere.

formation. However, evidence suggests that Tharsis was largely emplaced prior to the end of the late Noachian [*Phillips et al.*, 2001], and we show calculations that support the notion that sulfur volatiles in the atmosphere may prove necessary to create early warm, wet surface conditions. *Andrews-Hanna et al.* [2007a, 2007b] argue that surface runoff and shallow subsurface hydrology dominated aqueous geochemistry during this early period, with the combination of mildly acidic precipitation (a result of dissolved atmospheric sulfur volatiles) and weathering of surface basalts producing the observed early Noachian phyllosilicates [see also *Halevy et al.*, 2007]. This model suggests that sulfate evaporite deposition during the late Noachian or early Hesperian resulted not from a late stage injection of volcanic gases into the atmosphere but rather from a change in global hydrology in response to either a decrease in the total water inventory or an increase in the storage capacity of the crustal aquifers. The water table would have then dropped deep below the surface, and evaporation and precipitation rates would have become dictated by deep global-scale groundwater flow rates. As a result, mildly oxidizing fluids in deep basaltic aquifers would have reacted with pyrrhotite, creating significant acidity and liberating dissolved ferrous sulfate, and evaporite deposition would have become limited to isolated regions of groundwater upwelling, such as Meridiani Planum. A lessening of volcanic activity at the close of the late Noachian, and subsequent arid, low-temperature surface conditions in the absence of sulfur-related greenhouse warming, would have been part of this process.

[47] Large, sulfur-rich volcanic eruptions likely continued to occur through the Hesperian and into the Amazonian, though at a much lower rate than in the Noachian. Presumably, the thinner atmosphere resulted in cooler temperatures despite the added volcanic greenhouse effect (as in our 50 mbar simulations); nevertheless, later in Martian history there is evidence for the occurrence of transient warm climatic conditions, with valley network formation in the Hesperian and possibly Amazonian in some places [*Carr and Chuang*, 1997].

7. Conclusion

[48] There is substantial evidence for stable liquid water on the past surface of Mars, but the requisite environmental conditions are incompatible with the present climate. We

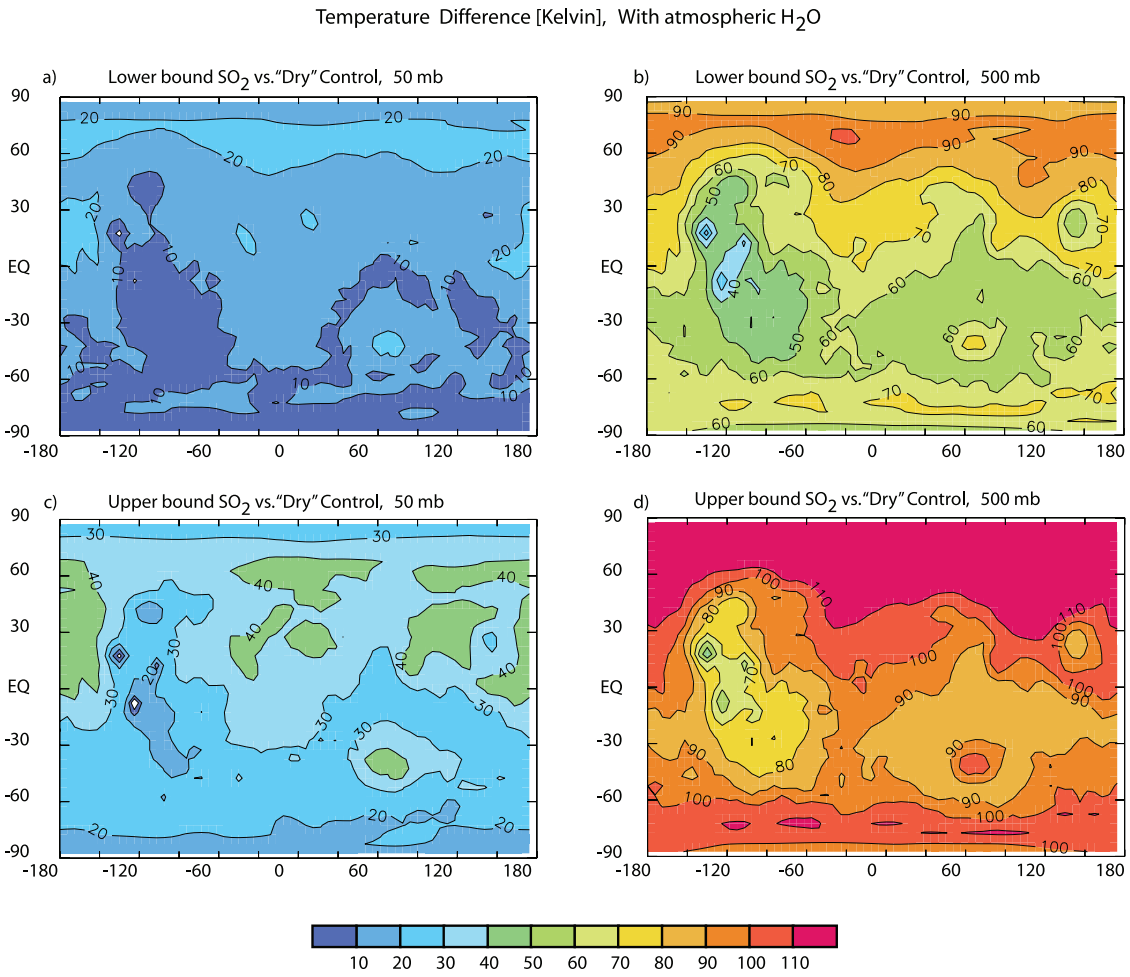

Figure 7. Difference (in kelvin) in annual average surface temperature between the "dry" control simulations (CO_2 only) and SO_2 pulse simulations, with the effects of water vapor, depicting the total warming from H_2O and CO_2. (a) Lower bound SO_2 abundance in 50 mbar atmosphere, b) lower bound SO_2 abundance in 500 mbar atmosphere, (c) upper bound SO_2 abundance in 50 mbar atmosphere, and (d) upper bound SO_2 abundance in 500 mbar atmosphere. This should be seen as an upper extreme in the absence of negative feedback mechanisms such as cloud cover.

hypothesize that large, episodic releases of sulfur volatiles early in the history of the planet could have generated up to 25 K of additional greenhouse warming, alone, over a large enough portion of the surface to drive, in tandem with water vapor feedbacks, dramatic climate fluctuations on early Mars. Degassing events of this magnitude could plausibly have occurred hundreds of times within the late Noachian. This scenario accords well with recent Mars mission findings, accounting for widespread geologic evidence for past stability of liquid water on early Mars, generation of surface acidity, preclusion of carbonate deposition, and high sulfur abundances as detected from orbit and at landing sites.

[49] **Acknowledgments.** We would like to thank J. Andrews-Hanna, R. Arvidson, J. Garvin, J. Grotzinger, J. Johnson, J. Lavinsky, A. Monders, A. Pavlov, L. Wilson, and the MER Science Team for insightful discussions. Support for S. Johnson was provided by a National Science Foundation Graduate Fellowship and a NASA Headquarters Planetary Geology and Geophysics Program to M. Zuber. Work by M. Mischna was performed at the Jet Propulsion Laboratory, California Institute of Technology, under a contract with the National Aeronautics and Space Administration. The climate simulations presented in this paper were performed on the supercomputing clusters at both JPL and the Caltech Division of Geological and Planetary Sciences.

References

Aharonson, O., M. T. Zuber, G. A. Neumann, and J. W. Head III (1998), Mars: Northern Hemisphere slopes and slope distributions, *Geophys. Res. Lett.*, *25*, 4413–4416, doi:10.1029/1998GL900057.

Andrews-Hanna, J. C., R. J. Phillips, and M. T. Zuber (2007a), Meridiani Planum and the global hydrology of Mars, *Nature*, *446*, 163–166, doi:10.1038/nature05594.

Andrews-Hanna, J. C., M. T. Zuber, and R. J. Phillips (2007b), Meridiani Planum: Implications for the hydrologic and climatic evolution of Mars, paper presented at Seventh International Conference on Mars, Jet Propul. Lab., Pasadena, Calif.

Arvidson, R. E., F. P. Seelos IV, K. S. Deal, W. C. Koeppen, N. O. Snider, J. M. Kieniewicz, B. M. Hynek, M. T. Mellon, and J. B. Garvin (2003), Mantled and exhumed terrains in Terra Meridiani, Mars, *J. Geophys. Res.*, *108*(E12), 8073, doi:10.1029/2002JE001982.

Arvidson, R. E., F. Poulet, J.-P. Bibring, M. Wolff, A. Gendrin, R. V. Morris, J. J. Freeman, Y. Langevin, N. Mangold, and G. Bellucci (2005), Spectral reflectance and morphologic correlations in eastern Terra Meridiani, Mars, *Science*, *307*, 1591–1594, doi:10.1126/science.1109509.

Baker, V. R., R. G. Strom, V. C. Gulick, J. S. Kargel, G. Komatsu, and V. S. Kale (1991), Ancient oceans, ice sheets and the hydrologic cycle on Mars, *Nature*, *352*, 589–594, doi:10.1038/352589a0.

Bandfield, J. L. (2002), Global mineral distributions on Mars, *J. Geophys. Res.*, *107*(E6), 5042, doi:10.1029/2001JE001510.
Banin, A. (2005), The enigma of the Martian soil, *Science*, *309*, 888–889, doi:10.1126/science.1112794.
Bertka, C. M., and J. R. Holloway (1994), Anhydrous partial melting of an iron-rich mantle II: Primary melt compositions at 15 kbar, *Contrib. Mineral. Petrol.*, *115*, 323–328, doi:10.1007/BF00310771.
Bibring, J.-P., et al. (2005), Mars surface diversity as revealed by the OMEGA/Mars Express observations, *Science*, *307*, 1576–1581, doi:10.1126/science.1108806.
Bibring, J.-P., et al. (2007), Mars climatic and geological history, derived from the OMEGA/MEX data, paper presented at Seventh International Conference on Mars, Jet Propul. Lab., Pasadena, Calif.
Blaney, D. L. (1996), Sulfate formation on Mars by volcanic aerosols: A new look, *Lunar Planet. Sci. Conf.*, *XXVII*, Abstract 123.
Bottinga, Y., and D. F. Weill (1970), Densities of liquid silicate systems calculated from partial molar volumes of oxide components, *Am. J. Sci.*, *269*, 169–182.
Brass, G. W. (1980), Stability of brines on Mars, *Icarus*, *42*, 20–28, doi:10.1016/0019-1035(80)90237-7.
Burt, D. M., L. P. Knauth, and K. H. Wohletz (2005), Origin of layered rocks, salts and spherules at the Opportunity landing site on Mars: No flowing or standing water evident or required, *Lunar Planet. Sci. Conf.*, *XXXVI*, Abstract 1527.
Carr, M. H., and F. C. Chuang (1997), Martian drainage densities, *J. Geophys. Res.*, *102*, 9145–9152, doi:10.1029/97JE00113.
Catling, D. C. (2008), Atmospheric evolution of Mars, in *Encyclopedia of Paleoclimatology and Ancient Environments*, edited by V. Gornitz, Kluwer Acad., New York, in press.
Christensen, P. R., et al. (2001), Mars Global Surveyor Thermal Emission Spectrometer experiment: Investigation description and surface science results, *J. Geophys. Res.*, *106*, 23,823–23,871, doi:10.1029/2000JE001370.
Clark, B. C., and D. C. Van Hart (1981), The salts of Mars, *Icarus*, *45*, 370–378, doi:10.1016/0019-1035(81)90041-5.
Clifford, S. M., and T. J. Parker (2001), The evolution of the Martian hydrosphere: Implications for the fate of a primordial ocean and the current state of the northern plains, *Icarus*, *154*, 40–79, doi:10.1006/icar.2001.6671.
Conrath, B. J. (1975), Thermal structure of the Martian atmosphere during the dissipation of the dust storm of 1971, *Icarus*, *24*, 36–46, doi:10.1016/0019-1035(75)90156-6.
DeMore, W. B., S. P. Sander, D. M. Golden, R. F. Hampson, M. J. Kurylo, C. J. Howard, A. R. Ravishankara, C. E. Kolb, and M. J. Molina (1997), Chemical kinetics and photochemical data for use in stratospheric modeling, Evaluation Number 12, *JPL Publ.*, *97-4*, 269 pp.
Dreibus, G., and H. Wanke (1985), Mars, a volatile-rich planet, *Meteoritics*, *20*(2), 367–381.
Edwards, J. M., and A. Slingo (1996), Studies with a flexible new radiation code. I: Choosing a configuration for a large-scale model, *Q. J. R. Meteorol. Soc.*, *122*, 689–719, doi:10.1002/qj.49712253107.
Fanale, F. P., S. E. Postawko, J. B. Pollack, and M. H. Carr (1992), Mars: Epochal climate change and volatile history, in *Mars*, edited by H. Kieffer et al., pp. 1135–1179, Univ. of Ariz. Press, Tucson.
Farquhar, J., J. Savrino, T. L. Jackson, and M. H. Thiemnes (2000), Evidence of atmospheric sulphur in the Martian regolith from sulphur isotopes in meteorites, *Nature*, *404*, 50–52, doi:10.1038/35003517.
Feldman, W. C., et al. (2004), Hydrated states of $MgSO_4$ at equatorial latitudes on Mars, *Geophys. Res. Lett.*, *31*, L16702, doi:10.1029/2004GL020181.
Fischer, J., R. R. Gamache, A. Goldman, L. S. Rothman, and A. Perrin (2003), Total internal partition sums for molecular species in the 2000 edition of the HITRAN database, *J. Quant. Spectrosc. Radiat. Transfer*, *82*, 401–412, doi:10.1016/S0022-4073(03)00166-3.
Flasar, F. M., and R. M. Goody (1976), Diurnal behavior of water on Mars, *Planet. Space Sci.*, *24*, 161–181, doi:10.1016/0032-0633(76)90103-3.
Forget, F., and R. T. Pierrehumbert (1997), Warming early Mars with carbon dioxide clouds that scatter infrared radiation, *Science*, *278*, 1273–1276, doi:10.1126/science.278.5341.1273.
Forget, F., F. Hourdin, R. Fournier, C. Hourdin, O. Talagrand, M. Collins, S. R. Lewis, P. L. Read, and J.-P. Huot (1999), Improved general circulation models of the Martian atmosphere from the surface to above 80 km, *J. Geophys. Res.*, *104*, 24,155–24,175, doi:10.1029/1999JE001025.
Fu, Q., and K. N. Liou (1992), On the correlated k-distribution method for radiative transfer in nonhomogeneous atmospheres, *J. Atmos. Sci.*, *49*, 2139–2156, doi:10.1175/1520-0469(1992)049<2139:OTCDMF>2.0.CO;2.
Gellert, R., et al. (2004), Chemistry of rocks and soils in Gusev Crater from the Alpha Particle X-ray Spectrometer, *Science*, *305*, 829–832, doi:10.1126/science.1099913.
Gendrin, A., et al. (2005), Sulfates in Martian layered terrains: The OMEGA/Mars Express view, *Science*, *307*, 1587–1591, doi:10.1126/science.1109087.
Gough, D. O. (1981), Solar interior structure and luminosity variations, *Sol. Phys.*, *74*, 21–34, doi:10.1007/BF00151270.
Greeley, R., B. H. Foing, H. Y. McSween, G. Neukum, P. Pinet, M. van Kan, S. C. Werner, D. A. Williams, and T. E. Zegers (2005), Fluid lava flows in Gusev Crater, Mars, *J. Geophys. Res.*, *110*, E05008, doi:10.1029/2005JE002401.
Gulick, V. C., D. Tyler, C. P. McKay, and R. M. Haberle (1997), Episodic ocean-induced CO_2 greenhouse on Mars: Implications for fluvial valley formation, *Icarus*, *130*, 68–86, doi:10.1006/icar.1997.5802.
Haberle, R. M., C. B. Leovy, and J. B. Pollack (1982), Some effects of global dust storms on the atmospheric circulation of Mars, *Icarus*, *50*, 322–367, doi:10.1016/0019-1035(82)90129-4.
Haberle, R. M., J. L. Hollingsworth, A. Colaprete, A. F. C. Bridger, C. P. McKay, J. R. Murphy, J. Schaeffer, and R. Freedman (2003), *The NASA Ames Mars General Circulation Model: Model Improvements and Comparison with Observations*, Mars Atmospheric Modeling and Observations Workshop, Granada, Spain.
Halevy, I., M. T. Zuber, and D. P. Schrag (2007), A sulfur dioxide climate feedback on early Mars, *Science*, *318*, 1903–1907, doi:10.1126/science.1147039.
Hanna, J. C., and R. J. Phillips (2006), Tectonic pressurization of aquifers in the formation of Mangala and Athabasca valles, Mars, *J. Geophys. Res.*, *111*, E03003, doi:10.1029/2005JE002546.
Head, J. W., III, H. Hiesinger, M. A. Ivanov, M. A. Kreslavsky, S. Pratt, and B. J. Thomson (1999), Possible ancient oceans on Mars: Evidence from Mars Orbiter Laser Altimeter data, *Science*, *286*, 2134–2137, doi:10.1126/science.286.5447.2134.
Held, I. M., and M. J. Suarez (1994), A proposal for the intercomparison of the dynamical cores of atmospheric general circulation models, *Bull. Am. Meteorol. Soc.*, *75*, 1825–1830, doi:10.1175/1520-0477(1994)075<1825:APFTIO>2.0.CO;2.
Holzheid, A., and T. L. Grove (2002), Sulfur saturation limits in silicate melts and their implications for core formation scenarios for terrestrial planets, *Am. Mineral.*, *87*, 227–237.
Hourdin, F. (1992), A new representation of the absorption by the CO_2 15-μm band for a Martian general circulation model, *J. Geophys. Res.*, *97*, 18,319–18,335.
Humlícek, J. (1982), Optimized computation of the Voigt and complex probability functions, *J. Quant. Spectrosc. Radiat. Transf.*, *27*, 437–444, doi:10.1016/0022-4073(82)90078-4.
Hynek, B. M., R. E. Arvidson, and R. J. Phillips (2002), Geologic setting and origin of Terra Meridiani hematite deposit on Mars, *J. Geophys. Res.*, *107*(E10), 5088, doi:10.1029/2002JE001891.
Johnson, S. S., M. T. Zuber, T. L. Grove, A. A. Pavlov, and M. A. Mischna (2007), Sulfur volatiles in the early Martian atmosphere, *Lunar Planet. Sci. Conf.*, *XXXVIII*, Abstract 1754.
Kasting, J. F. (1991), CO_2 condensation and the climate of early Mars, *Icarus*, *94*, 1–13, doi:10.1016/0019-1035(91)90137-I.
Kasting, J. F. (1997), Warming early Earth and Mars, *Science*, *276*, 1213–1215, doi:10.1126/science.276.5316.1213.
Knoll, A. H., et al. (2005), An astrobiological perspective on Meridiani Planum, *Earth Planet. Sci. Lett.*, *240*, 179–189, doi:10.1016/j.epsl.2005.09.045.
Lacis, A. A., and V. Oinas (1991), A description of the correlated *k* distribution method for modeling nongray gaseous absorption, thermal emission and multiple scattering in vertically inhomogeneous atmospheres, *J. Geophys. Res.*, *96*, 9027–9063, doi:10.1029/90JD01945.
Lemmon, E. W., M. O. McLinden, and D. G. Friend (2005), Thermophysical properties of fluid systems, in *NIST Chemistry WebBook, NIST Standard Reference Database Number 69*, edited by P. J. Linstrom and W. G. Mallard, Natl. Inst. of Stand. and Technol., Gaithersburg, Md. (Available at http://webbook.nist.gov/chemistry/fluid/)
Maguire, W. S. (1977), Martian isotopic ratios and upper limits for possible minor constituents as derived from Mariner 9 infrared spectrometer data, *Icarus*, *32*, 85–97, doi:10.1016/0019-1035(77)90051-3.
Mavrogenes, J. A., and H. S. C. O'Neill (1999), The relative effects of pressure, temperature and oxygen fugacity on the solubility of sulfide in mafic magmas, *Geochim. Cosmochim. Acta*, *63*, 1173–1180, doi:10.1016/S0016-7037(98)00289-0.
McLennan, S. M., et al. (2005), Provenance and diagenesis at Meridiani Planum, *Earth Planet. Sci. Lett.*, *240*, 95–121, doi:10.1016/j.epsl.2005.09.041.
McSween, H. Y., Jr., et al. (2006), Characterization and petrologic interpretation of olivine-rich basalts at Gusev Crater, Mars, *J. Geophys. Res.*, *111*, E02S10, doi:10.1029/2005JE002477.
Mills, K. C. (1993), The influence of structure on the physico-chemical properties of slags, *ISIJ Int.*, *33*, 148–155, doi:10.2355/isijinternational.33.148.

Mischna, M. A., J. F. Kasting, A. Pavlov, and R. Freedman (2000), Influence of carbon dioxide clouds on early Martian climate, *Icarus*, *145*, 546–554, doi:10.1006/icar.2000.6380.

Mo, X., I. S. E. Carmichael, M. Rivers, and J. Stebbins (1982), The partial molar volume of Fe_2O_3 in multicomponent silicate liquids and the pressure dependence of oxygen fugacity in magmas, *Mineral. Mag.*, *45*, 237–245, doi:10.1180/minmag.1982.045.337.27.

Monders, A. G., E. Medard, and T. L. Grove (2007), Phase equilibrium investigations of the Adirondack class basalts from the Gusev plains, Gusev Crater, Mars, *Meteorit. Planet. Sci.*, *42*, 131–148.

Montmessin, F., F. Forget, P. Rannou, M. Cabane, and R. M. Haberle (2004), Origin and role of water ice clouds in the Martian water cycle as inferred from a general circulation model, *J. Geophys. Res.*, *109*, E10004, doi:10.1029/2004JE002284.

Mysen, B. O. (1988), *Structure and Properties of Silicate Melts*, *Dev. Geochem.*, vol. 4, 368 pp., Elsevier, New York.

Owen, T. (1992), The composition and early history of the atmosphere of Mars, in *Mars*, edited by H. Kieffer et al., pp. 818–834, Univ. of Ariz. Press, Tucson.

Pavlov, A. A., and J. F. Kasting (2002), Mass-independent fractionation of sulfur isotopes in Archean sediments: Strong evidence for an anoxic Archean atmosphere, *Astrobiology*, *2*, 27–41, doi:10.1089/153110702753621321.

Perron, J. T., J. X. Mitrovica, M. Manga, I. Matsuyama, and M. A. Richards (2007), Evidence for an ancient Martian ocean in the topography of deformed shorelines, *Nature*, *447*, 840–843, doi:10.1038/nature05873.

Phillips, R. J., et al. (2001), Ancient geodynamics and global-scale hydrology on Mars, *Science*, *291*, 2587–2591, doi:10.1126/science.1058701.

Pollack, J. B., J. F. Kasting, S. M. Richardson, and K. Poliakoff (1987), The case for a wet, warm climate on early Mars, *Icarus*, *71*, 203–224, doi:10.1016/0019-1035(87)90147-3.

Postawko, S. E., and W. R. Kuhn (1986), Effect of the greenhouse gases (CO_2, H_2O, SO_2) on Martian paleoclimate, *Proc. Lunar Planet. Sci. Conf. 16th, Part 2*, *J. Geophys. Res.*, *91, suppl.*, D431–D438, doi:10.1029/JB091iB04p0D431.

Putzig, N. E., M. T. Mellon, K. A. Kretke, and R. E. Arvidson (2005), Global thermal inertia and surface properties of Mars from the MGS mapping mission, *Icarus*, *173*, 325–341, doi:10.1016/j.icarus.2004.08.017.

Richardson, M. I., and M. A. Mischna (2005), The long-term evolution of transient liquid water on Mars, *J. Geophys. Res.*, *110*, E03003, doi:10.1029/2004JE002367.

Richardson, M. I., A. D. Toigo, and C. E. Newman (2007), PlanetWRF: A general purpose, local to global numerical model for planetary atmospheric and climate dynamics, *J. Geophys. Res.*, *112*, E09001, doi:10.1029/2006JE002825.

Roach, L. H., et al. (2007), CRISM spectral signatures of the north polar gypsum dunes, *Lunar Planet. Sci. Conf.*, *XXXVIII*, Abstract 1970.

Rothman, L. S., et al. (2005), The HITRAN 2004 molecular spectroscopic database, *J. Quant. Spectrosc. Radiat. Transfer*, *96*, 139–204, doi:10.1016/j.jqsrt.2004.10.008.

Rutherford, M. J., M. Minitti, and C. M. Weitz (2001), Compositions of Mars rocks: SNC meteorites, differentiates and soils, paper presented at Workshop on Mars 2001: Integrated Science in Preparation for Sample Return and Human Exploration, Lunar and Planet. Inst., Houston, Tex.

Sagan, C., and C. Chyba (1997), The early faint Sun paradox: Organic shielding of ultraviolet-labile greenhouse gases, *Science*, *276*, 1217–1221, doi:10.1126/science.276.5316.1217.

Scott, E. D., L. Wilson, and J. W. Head III (2002), Emplacement of giant radial dikes in the northern Tharsis region of Mars, *J. Geophys. Res.*, *107*(E4), 5019, doi:10.1029/2000JE001431.

Segura, T. L., O. B. Toon, A. Coloprete, and K. Zahnle (2002), Environmental effects of large impacts on Mars, *Science*, *298*, 1977–1980, doi:10.1126/science.1073586.

Settle, M. (1979), Formation and deposition of volcanic sulfate aerosols on Mars, *J. Geophys. Res.*, *84*, 8343–8354, doi:10.1029/JB084iB14p08343.

Smith, M. D., J. C. Pearl, B. J. Conrath, and P. R. Christensen (2001), Thermal Emission Spectrometer results: Mars atmospheric thermal structure and aerosol distribution, *J. Geophys. Res.*, *106*, 23,929–23,945, doi:10.1029/2000JE001321.

Squyres, S. W., et al. (2004), The Opportunity Rover's Athena science investigation at Meridiani Planum, Mars, *Science*, *306*, 1698–1703, doi:10.1126/science.1106171.

Thordarson, T., and S. Self (2003), Atmospheric and environmental effects of the 1783–1784 Laki eruption: A review and reassessment, *J. Geophys. Res.*, *108*(D1), 4011, doi:10.1029/2001JD002042.

Wadhwa, M. (2001), Redox states of Mars' upper mantle and crust from Eu anomalies in shergottite pyroxenes, *Science*, *291*, 1527–1530, doi:10.1126/science.1057594.

Wänke, H., J. Bruckner, G. Dreibus, R. Rieder, and I. Ryanchikov (2001), Chemical composition of rocks and soils at the Pathfinder site, *Space Sci. Rev.*, *96*, 317–330, doi:10.1023/A:1011961725645.

Wilson, L., and J. W. Head III (2002), Tharsis-radial graben systems as the surface manifestation of plume-related dike intrusion complexes: Models and implications, *J. Geophys. Res.*, *107*(E8), 5057, doi:10.1029/2001JE001593.

Wilson, R. J., and K. Hamilton (1996), Comprehensive model simulation of thermal tides in the Martian atmosphere, *J. Atmos. Sci.*, *53*, 1290–1326, doi:10.1175/1520-0469(1996)053<1290:CMSOTT>2.0.CO;2.

Wong, A.-S., S. K. Atreya, and T. Encrenaz (2004), Correction to "Chemical markers of possible hot spots on Mars," *J. Geophys. Res.*, *109*, E01007, doi:10.1029/2003JE002210.

Wong, A.-S., S. K. Atreya, and T. Encrenaz (2005), Correction to and updated reaction in "Chemical markers of possible hot spots on Mars," *J. Geophys. Res.*, *110*, E10002, doi:10.1029/2005JE002509.

Yen, A. S., et al. (2005), An integrated view of the chemistry and mineralogy of Martian soils, *Nature*, *436*, 49–54, doi:10.1038/nature03637.

Yung, Y., H. Nair, and M. E. Gerstell (1997), CO_2 greenhouse in the early Martian atmosphere: SO_2 inhibits condensation, *Icarus*, *130*, 222–224, doi:10.1006/icar.1997.5808.

Zahnle, K. J., and R. M. Haberle (2006), Atmospheric sulfur chemistry on ancient Mars, paper presented at Workshop on Martian Sulfates as Recorders of Atmospheric-Fluid-Rock Interactions, Lunar and Planet. Inst., Houston, Tex.

Zolotov, M. Y., and E. L. Shock (2005), Formation of jarosite-bearing deposits through aqueous oxidation of pyrite at Meridiani Planum, Mars, *Geophys. Res. Lett.*, *32*, L21203, doi:10.1029/2005GL024253.

Zuber, M. T. (2001), The crust and mantle of Mars, *Nature*, *412*, 220–227, doi:10.1038/35084163.

T. L. Grove, S. S. Johnson, and M. T. Zuber, Department of Earth, Atmospheric and Planetary Science, Massachusetts Institute of Technology, 77 Massachusetts Avenue, Cambridge, MA 02139, USA. (ssj@mit.edu)

M. A. Mischna, Jet Propulsion Laboratory, California Institute of Technology, M/S 183-401, 4800 Oak Grove Drive, Pasadena, CA 91109, USA.